OPEN ACCESS

ARTICLE

Deciphering the synergistic mechanism for thermal stability improvement in Ni-rich single-crystal cathode materials *via* $LiNbO_3$ coating and Nb^{5+} surface doping

Zesen Wei,[1,5] Zheng Fang,[1,5] Chen Liang,[1,3] Shiyao Chen,[1] Anqi Teng,[1] Mei Sun,[2] Yue Zhang,[1] Yin Yu,[1] Xiangdong Meng,[1] Peiyu Duan,[1] Lihua Jiang,[1,4] Jinhua Sun,[1,*] and Qingsong Wang[1,*]

*Correspondence: sunjh@ustc.edu.cn(J. S.); pinew@ustc.edu.cn(Q. W.)

Received: October 29, 2024; Accepted: December 10, 2024; https://doi.org/10.59717/j.xinn-energy.2025.100083

GRAPHICAL ABSTRACT

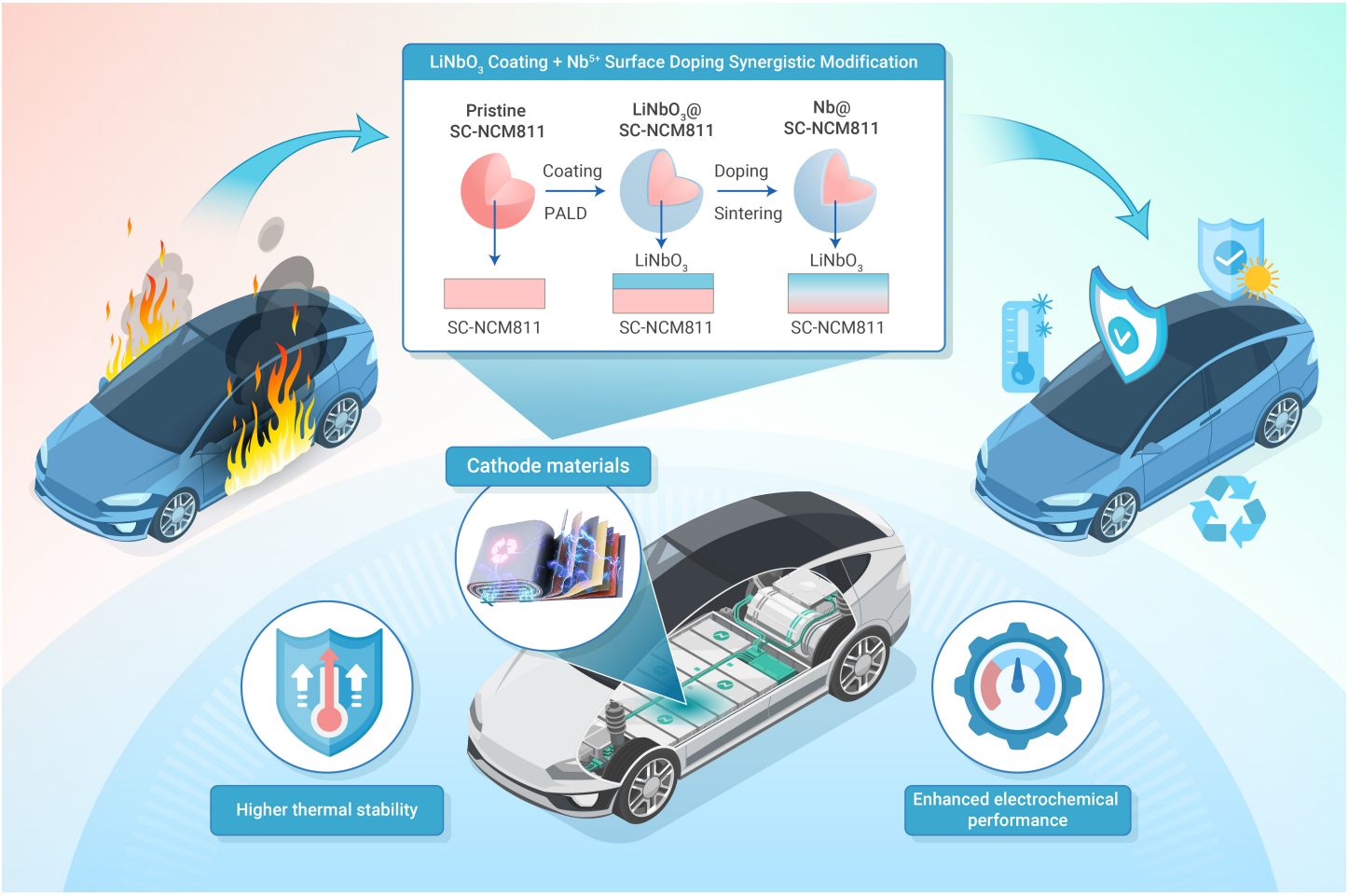

PUBLIC SUMMARY

- Ni-rich cathodes' thermal stability improved by $LiNbO_3$ coating and Nb^{5+} doping.
- Nb@SC-NCM811 shows better electrochemical performance and higher thermal stability.
- Enhanced stability due to oxygen vacancy formation and increased migration barrier.

ARTICLE

OPEN ACCESS

Deciphering the synergistic mechanism for thermal stability improvement in Ni-rich single-crystal cathode materials *via* $LiNbO_3$ coating and Nb^{5+} surface doping

Zesen Wei,[1,5] Zheng Fang,[1,5] Chen Liang,[1,3] Shiyao Chen,[1] Anqi Teng,[1] Mei Sun,[2] Yue Zhang,[1] Yin Yu,[1] Xiangdong Meng,[1] Peiyu Duan,[1] Lihua Jiang,[1,4] Jinhua Sun,[1,*] and Qingsong Wang[1,*]

[1]State Key Laboratory of Fire Science, University of Science and Technology of China, Hefei 230026, China

[2]Instrument Center for Physical Science, University of Science and Technology of China, Hefei 230026, China

[3]School of Safety Science and Engineering, Changzhou University, Changzhou 213164, China

[4]College of Safety and Environmental Engineering, Shandong University of Science and Technology, Qingdao, 266590, China

[5]These authors contributed equally

*Correspondence: sunjh@ustc.edu.cn(J. S.); pinew@ustc.edu.cn(Q. W.)

Received: October 29, 2024; Accepted: December 10, 2024; https://doi.org/10.59717/j.xinn-energy.2025.100083

Citation: Wei Z., Fang Z., Liang C., et al. (2025). Deciphering the synergistic mechanism for thermal stability improvement in Ni-rich single-crystal cathode materials *via* $LiNbO_3$ coating and Nb^{5+} surface doping. *The Innovation Energy* **2**:100083.

Ni-rich cathode materials are highly regarded for their potential in high-energy density lithium-ion batteries (LIBs). Nonetheless, their intrinsic thermal instability poses a significant risk of thermal runaway, which is a major obstacle to their commercial application. This study presents a novel approach to enhancing the thermal stability of Ni-rich cathode materials for LIBs through a synergistic modification strategy combining $LiNbO_3$ coating and Nb^{5+} surface doping. By applying particle atomic layer deposition and high-temperature sintering, the modified cathode material Nb@SC-NCM811 shows better electrochemical performance. Thermal analysis reveals that Nb@SC-NCM811 has a higher thermal decomposition temperature, generates less heat, and releases less oxygen under thermal induction, indicating enhanced thermal stability. The microscopic mechanisms underlying the improvement of thermal stability are further revealed through aberration-corrected transmission electron microscopy and density functional theory calculations, which shows that the enhancement in thermal stability is due to the increased formation energy of oxygen vacancies and the raised energy barrier for interlayer migration of transition metal cations. This work provides insight into the Nb-modified mechanism of Ni-rich cathode materials and offers a promising avenue for designing safer, high-energy density LIBs.

INTRODUCTION

Lithium-ion batteries (LIBs) have emerged as a predominant choice for energy storage, propelled by the swift advancement of portable electronics, electric vehicles (EVs), and energy storage systems (ESS). Due to their higher energy density and electrochemical performance, layered cathode materials, nickel-cobalt-manganese (NCM) ternary cathode materials, have emerged as a focal point in LIBs research and applications.[1] Ni-rich cathode materials enhance the energy density by increasing nickel content while reducing cobalt content, thereby achieving higher energy density and lowering the overall cost, presenting broad development prospects.[2] However, LIBs with Ni-rich cathode materials are more prone to thermal runaway under abuse conditions, raising serious safety concerns.[3,4] The inferior thermal stability of Ni-rich cathode materials is a principal factor contributing to the increased risk of thermal runaway. As nickel content increases, the cathode material is more likely to decompose upon heating,[5] generating heat at lower temperatures and releasing substantial oxygen.[6] The released oxygen reacts with the internal electrolyte and other combustible gases in the battery, producing significant heat and causing combustion, which in turn accelerates the process of thermal runaway.[7] This susceptibility is attributed to the transition metal (TM) cations (mainly Ni and Co) in Ni-rich cathode materials being more readily reduced to a lower valence state, accompanied by a transformation in the crystal structure, the release of oxygen, and the generation of heat.[8-10]

In recent years, researchers have proposed various modification strategies to improve the overall performance of LIBs including thermal safety.[11-13] Coating cathode materials with a nanometer-thick layer of metal oxides[14-17] or ion-conducting oxides[18-21] can significantly reduce the side reactions between the electrolyte and the cathode, improving the chemical stability of the cathode material interface. This enhancement increases reversible capacity and maintains the battery's long-term cycling performance. Additionally, doping strategies,[22-25] particularly through precise concentration and distribution control of doping elements (such as gradient doping[26,27] and surface doping[28]), have been proven to suppress the migration of TM ions from the TM layer to the Li layer during cycling, thereby stabilizing the layered structure of NCM cathode materials. Doping strategies have also played a pivotal role in improving the LIB's rate performance and cycle life.[29] Furthermore, recent studies have revealed that doping cathode materials with high-valence elements, such as Nb^{5+}, Ta^{5+}, Mo^{6+}, and W^{6+}, significantly enhances electrochemical performance compared to some low-valence elements (Mg^{2+}, Al^{3+}, Zr^{4+}, and Ti^{4+}).[30] Despite numerous studies focusing on the structural modification of Ni-rich cathode materials to enhance electrochemical performance, exploration into their thermal stability and overall thermal safety remains insufficient. Therefore, the structural modification strategies for improving the thermal stability of Ni-rich cathode materials and their corresponding mechanisms require further in-depth investigation.

This work focuses on the optimization and modification for enhancing the thermal stability of Ni-rich cathode materials (Single-crystal NCM811, SC-NCM811). Powder atomic layer deposition (PALD) is recognized for its ability to create uniform and precise coatings at the atomic level, making it a valuable technique for modifying LIBs cathode materials. With innovative reactor designs, such as fluidized bed reactors (FBR) and rotary reactors, PALD now enables conformal coatings on large quantities of particles, ensuring uniformity and efficiency.[31] Furthermore, high-throughput PALD systems, capable of processing up to 30,000 kg of powder per day, have demonstrated their economic viability, with costs as low as $1 per kilogram.[32] Herein, the $LiNbO_3$ coating and Nb^{5+} surface doping Nb@SC-NCM811 cathode materials were synthesized by commercial PALD system and optimized post-annealing process. Nb@SC-NCM811 exhibits improved electrochemical performance, especially regarding the capacity retention of LIBs under extended cycling conditions. Furthermore, the improvement in thermal stability of the Nb@SC-NCM811 cathode material was verified through thermal analysis characterization techniques. Finally, through characterization experiments with spherical aberration-corrected scanning transmission electron microscopic (AC-STEM) and density functional theory (DFT) calculations, the microscopic mechanism of Nb-modification to improve the thermal stability of LIBs has been revealed. In summary, the $LiNbO_3$ coating and Nb^{5+} surface doping synergistic modification strategy effectively enhances the thermal stability of NCM811 cathode materials and improves the overall thermal safety of LIBs, which provides a crucial scientific foundation for designing safer high-energy density LIBs.

MATERIALS AND METHODS

$LiNbO_3$ was uniformly coated on the SC-NCM811 surface using a commercial PALD system with 20 growth cycles, followed by Nb^{5+} surface

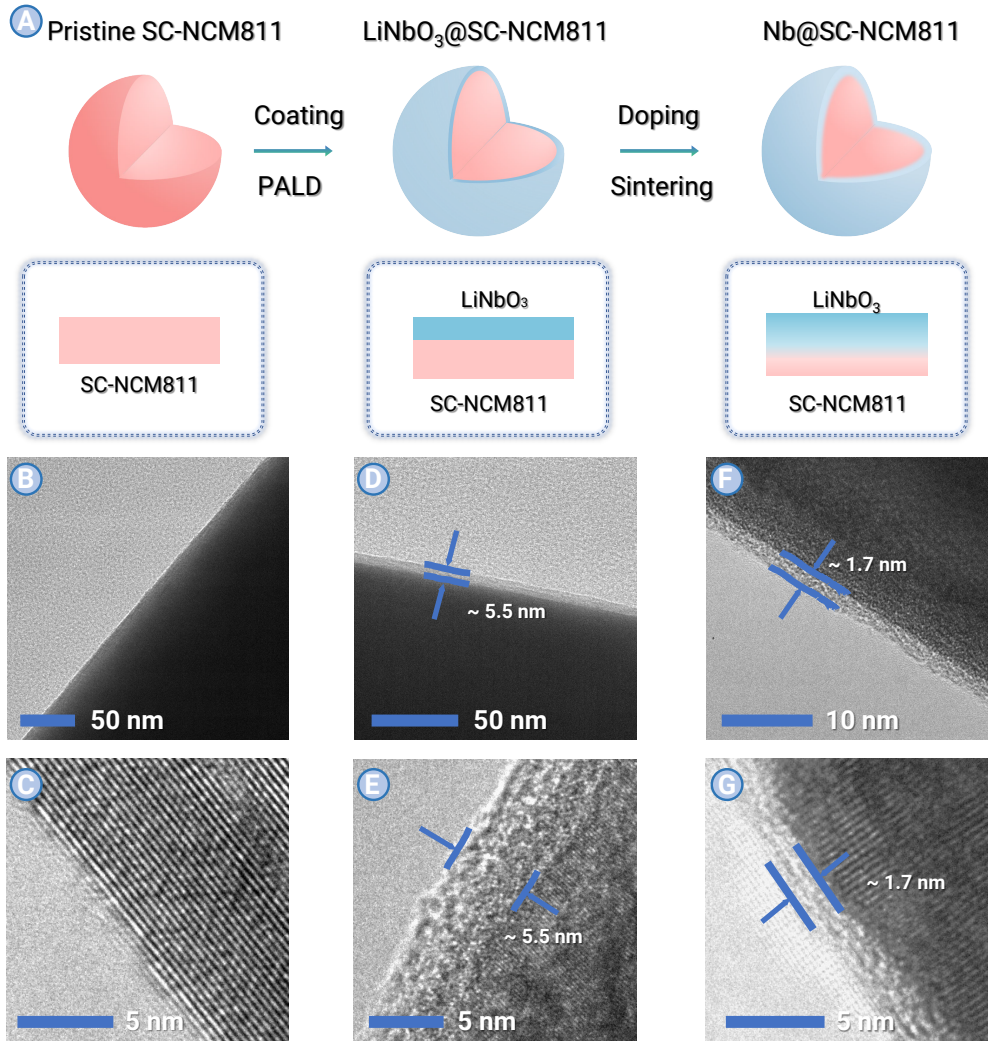

Figure 1. (A) Modification strategy of $LiNbO_3$ coating and Nb^{5+} surface doping for the Pristine SC-NCM811. TEM images and HR-TEM images of Ni-rich cathode materials. (B & C) Pristine SC-NCM811. (D & E) $LiNbO_3$@SC-NCM811. (F & G) Nb@SC-NCM811

doping *via* sintering in an oxygen atmosphere at 700 °C (Figure S1). XRD measurement was conducted within the 2-theta range of 10–80° using a Rigaku SmartLab9 (Cu Kα). The prepared cathode materials, SC-NCM811 and Nb@SC-NCM811, were then fabricated into CR2032 coin cells and pouch cells, with the former involving a mixture of cathode material, carbon black, and PVDF binder in an 8:1:1 ratio, coated on aluminum foil, and paired with a lithium metal anode and 1 M $LiPF_6$ in EC/DEC (volume ratio 1:1) electrolyte. Pouch cells followed a similar protocol but were adjusted for larger-scale assembly. Electrochemical performance testing of coin cells was conducted at 30 °C, with initial cycling at 0.1 C followed by 0.5 C and additional tests at 1 C to compare cycling performance. Thermal stability of both the cathode materials and cathode-electrolyte system was assessed with thermogravimetric analysis-differential scanning calorimetry (TGA-DSC), thermogravimetry-mass spectrometry (TG-MS), and C80 micro-calorimetry at the material level. The heat generation process during the charge-discharge cycle of coin cells was investigated using a multiple module calorimeter (MMC), and accelerating rate calorimetry (ARC) was used to study the thermal runaway process of pouch cells in an adiabatic environment. Material structural and compositional analyses were performed on the cathode particles using high-resolution TEM (HR-TEM) and EDS, with further atomic-scale examination using AC-STEM following focused ion beam (FIB) sectioning. Additionally, DFT calculations were carried out using Vienna Ab-initio Simulation Package (VASP) to investigate oxygen vacancy formation energy and TM element interlayer migration barriers. Detailed experimental descriptions are provided in the supplemental materials.

RESULTS AND DISCUSSION

Validation of the effectiveness of $LiNbO_3$ coating and Nb^{5+} surface doping

Firstly, the effectiveness and synergistic effects of Nb-modification on Ni-rich cathode materials were explored. As shown in Figure 1A, based on the Pristine SC-NCM811 cathode material, $LiNbO_3$ coating is designed by PALD method ($LiNbO_3$@SC-NCM811), as well as achieving $LiNbO_3$ coating and Nb^{5+} surface doping after subsequent high-temperature sintering (Nb@SC-NCM811). Figures 1B-G illustrate the microstructural evolution of the Ni-rich cathode material from Pristine SC-NCM811, to $LiNbO_3$ coated $LiNbO_3$@SC-NCM811, and then to $LiNbO_3$ coated-Nb^{5+} surface doped Nb@SC-NCM811. As depicted in Figure 1D, a coating layer with ~5.5 nm thickness emerges on the surface of the single-crystal cathode particles following the PALD process. Subsequent high-temperature sintering facilitates the surface doping of Nb^{5+} from the coating layer into the particle interior, significantly reducing the thickness of the coating layer to below 2 nm (Figure 1F), thereby achieving a synergistic modification effect through $LiNbO_3$ coating and Nb^{5+} surface doping. Furthermore, HR-TEM was used to characterize the structural properties of the Pristine SC-NCM811 at various modification stages. Figure 1C shows the presence of distinct lattice fringes on the edge surface of the Pristine SC-NCM811 without any amorphous phase. After the PALD coating process, the high-resolution image in Figure 1E shows that the outermost layer of the lattice fringes is covered by an amorphous layer approximately 5 nm thick. Following the high-temperature sintering process, Nb@SC-NCM811 still exhibits clear layered lattice fringes (Figure 1G), indicating that high-temperature sintering of $LiNbO_3$@SC-NCM811 in an oxygen atmosphere does not compromise the layered structure of the cathode particles. In addition, it is found that the coating thickness of Nb@SC-NCM811 significantly reduces after sintering, implying that part of the $LiNbO_3$ coating layer is doped into the surface layer of the cathode particles under high temperatures.

To intuitively investigate the modification effects of coating and surface doping in the Pristine SC-NCM811, the energy dispersive spectroscopy mapping function (EDS-Mapping) was used to explore the two-dimensional distribution of Nb elements at different modification stages. Figures S2A-C visually demonstrate the highly concentrated distribution of Nb elements on the surface layer of the cathode particles ($LiNbO_3$@SC-NCM811), forming a distinct bright edge, which corresponds to the $LiNbO_3$ coating with a thickness similar to that of the amorphous film layer observed under TEM mode (approximately 5 nm). Compared to the $LiNbO_3$@SC-NCM811, the distribution of Nb elements in the Nb@SC-NCM811 exhibits a more significant difference. Figures S2D-F show that the Nb element is not highly concentrated at the surface edge but is more uniformly distributed from the particle surface inward in the Nb@SC-NCM811. After overlaying the distribution map with Ni elements, it is noticeable that the Nb element is still relatively concentrated at the edges surface of the cathode particles, indicating that part of the $LiNbO_3$ coating layer was retained during the high-temperature sintering process. This phenomenon further validates the effectiveness of the $LiNbO_3$ coating and Nb^{5+} surface doping modification strategy presented in this work.

Moreover, cross-sectional images of the cathode material provide a more

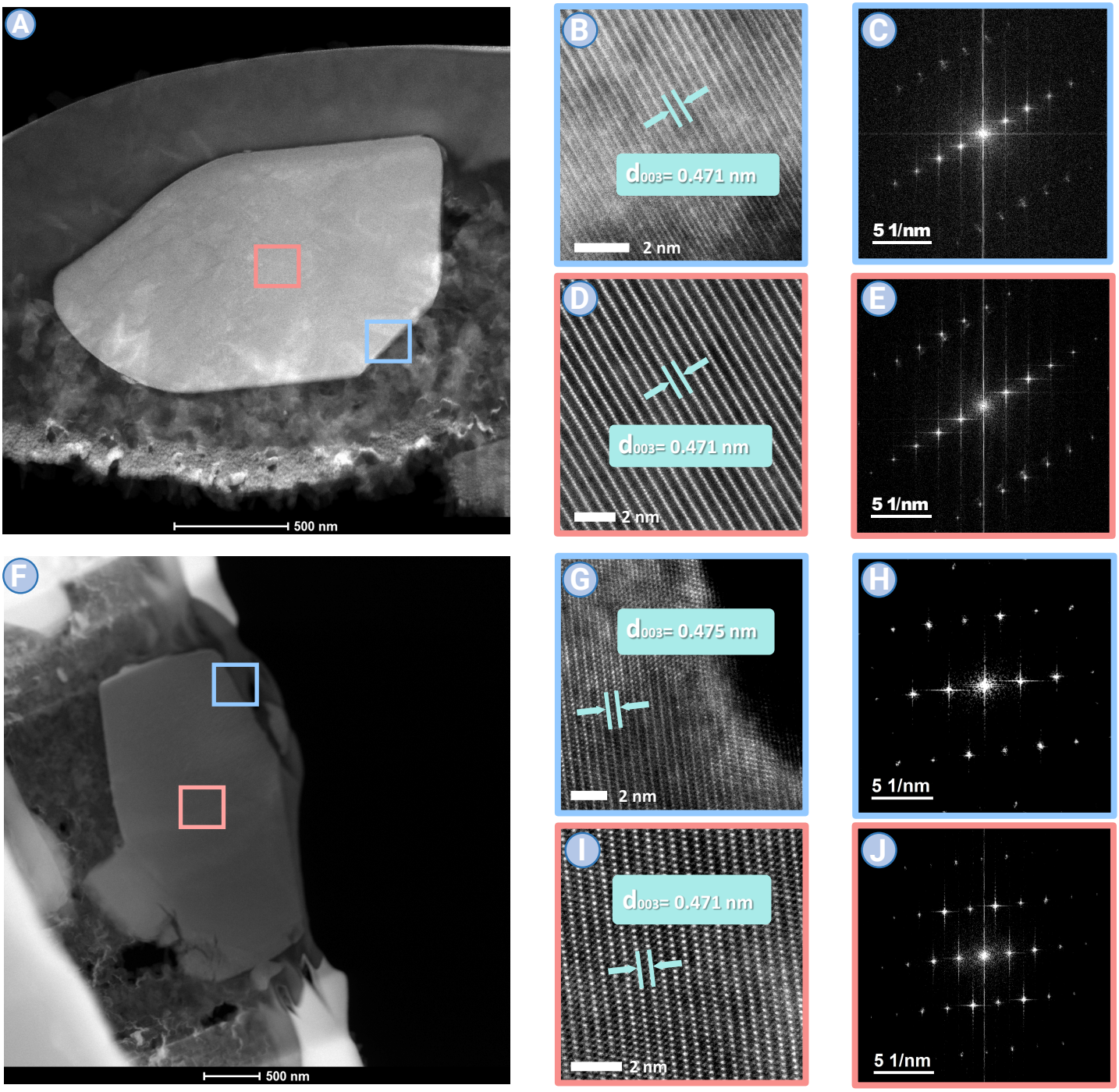

Figure 2. (A) HAADF-STEM image of $LiNbO_3$@SC-NCM811, atomic arrangement images and corresponding FFT patterns of (B & C) surface region, and (D & E) bulk region; (F) HAADF-STEM image of Nb@SC-NCM811 cathode particles, atomic arrangement images and corresponding FFT patterns of (G & H) surface region, and (I & J) bulk region.

direct and reliable method for analyzing the effects of coating and surface doping.[33] To achieve this, FIB and AC-STEM techniques were employed to delve deeper into the effects of Nb-modification strategies on the lattice structure of SC-NCM811. As shown in Figures 2, the differences in the lattice spacing of TM layers between the surface and bulk regions of $LiNbO_3$@SC-NCM811 and Nb@SC-NCM811 are further compared, leading to the inference that Nb^{5+} doping occurs only in the surface region of the cathode material. As depicted in Figures 2A-E, the surface and bulk of $LiNbO_3$@SC-NCM811 exhibit a well-defined layered structure. The lattice spacing for the (003) crystal planes is annotated by performing the Fast Fourier Transform (FFT) on the atomic arrangement images. It is found that the lattice spacing of crystal planes in both the surface and bulk of $LiNbO_3$@SC-NCM811 is 0.471 nm, indicating that the PALD coating process has no impact on the atomic arrangement of TM atoms within the cathode material. However, for Nb@SC-NCM811 cathode particles (Figures 2F-J), the lattice spacing of crystal planes at the surface increases from 0.471 nm to 0.475 nm, which is attributed to the larger atomic radius of Nb^{5+} (0.64 Å) compared to Ni^{3+} (0.56 Å), Co^{3+} (0.54 Å), and Mn^{4+} (0.53 Å).[29] When Nb^{5+} is doped into the layered structure of SC-NCM811, it expands the lattice spacing within the TM layers.[29] As evident from Figure 2I, the lattice spacing in the bulk region of Nb@SC-NCM811 remains at 0.471 nm, indicating that Nb^{5+} is not doped into the bulk region of the cathode particles. Therefore, the experimental results adequately demonstrate that Nb^{5+} doping is confined to the surface layer of SC-NCM811, achieving the anticipated surface doping effect.

Electrochemical performance of Nb@SC-NCM811

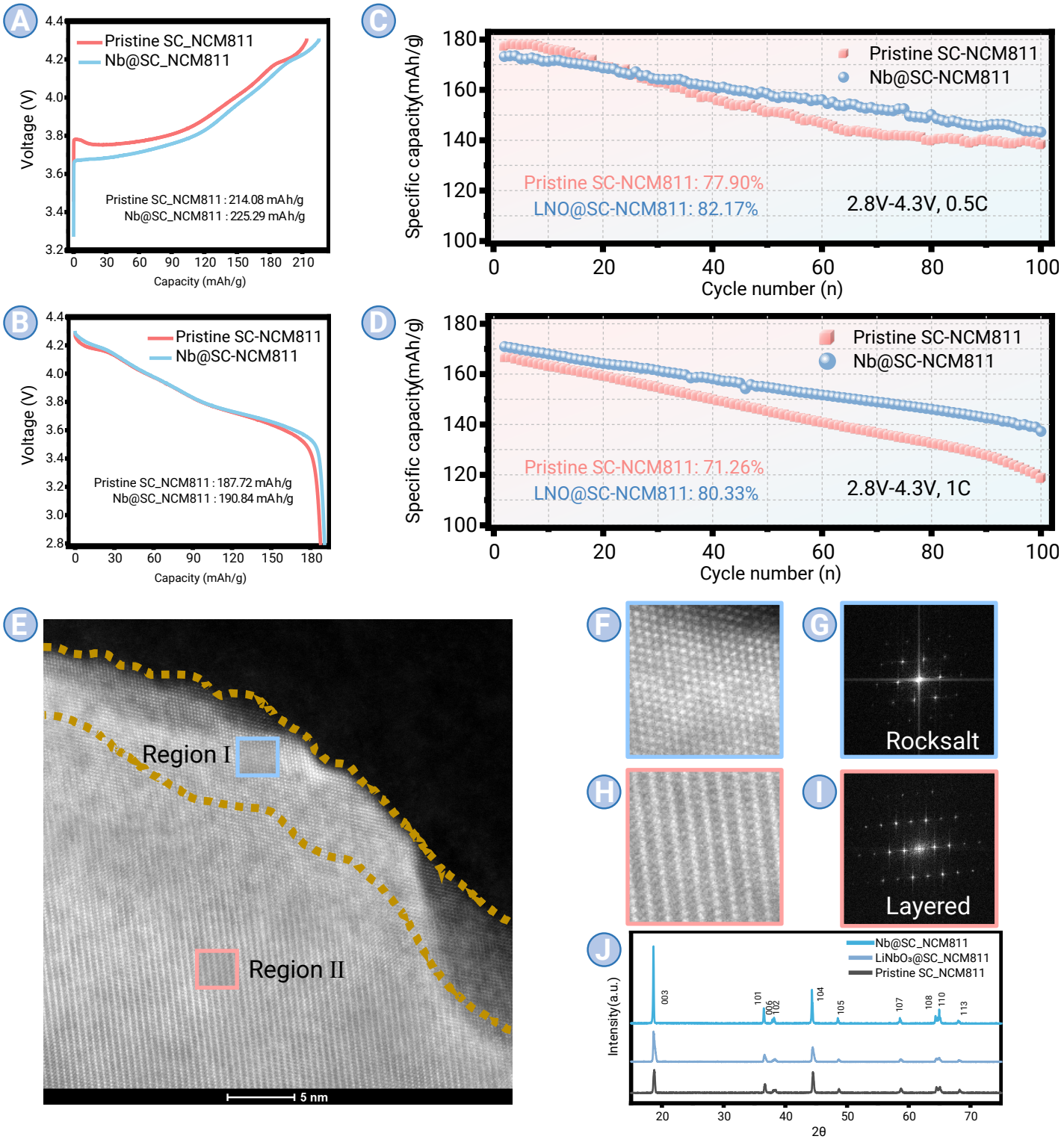

Figure 3. Electrochemical performance of Pristine SC-NCM811 and Nb@SC-NCM811 (A) First charge curve and (b) First discharge curve at 0.1C, 2.8-4.3 V, 30 °C. Cycling performance at (C) 0.5C and (D) 1C for 100 cycles, 30 °C. (E) HAADF-STEM image of Nb@SC-NCM811 in the surface and bulk regions. (F) Atomic arrangement image of Region I, and (G) corresponding FFT image. (H) Atomic arrangement image of Region II, and (I) corresponding FFT image. (J) XRD patterns of Pristine SC-NCM811, $LiNbO_3$@SC-NCM811, and Nb@SC-NCM811

The cycling performance of the Pristine SC-NCM811 and Nb@SC-NCM811 was evaluated in a voltage range of 2.8-4.3 V at 0.5 and 1 C after one activation cycle at C/10. Figure 3A-B display the voltage variation with specific capacity during the first charge and discharge processes for the Pristine SC-NCM811 and Nb@SC-NCM811, respectively. As shown in Figure 3A, the charging specific capacity of Pristine SC-NCM811 is 214.08 mAh/g, whereas that of Nb@SC-NCM811 is 225.29 mAh/g. Nb@SC-NCM811 exhibits a lower voltage plateau and weaker polarization phenomenon at the beginning of charging, which explains the increase in charging specific capacity for the Nb-modified cathode material.[34] Figure 3B shows the first discharge process of the two cathode materials, where Nb@SC-NCM811 undergoes a slower self-discharge process after reaching the cut-off voltage (2.8 V), and its discharge specific capacity (190.84 mAh/g) is higher than that of Pristine SC-NCM811 (187.72 mAh/g). The improvement in the electrochemical performance of

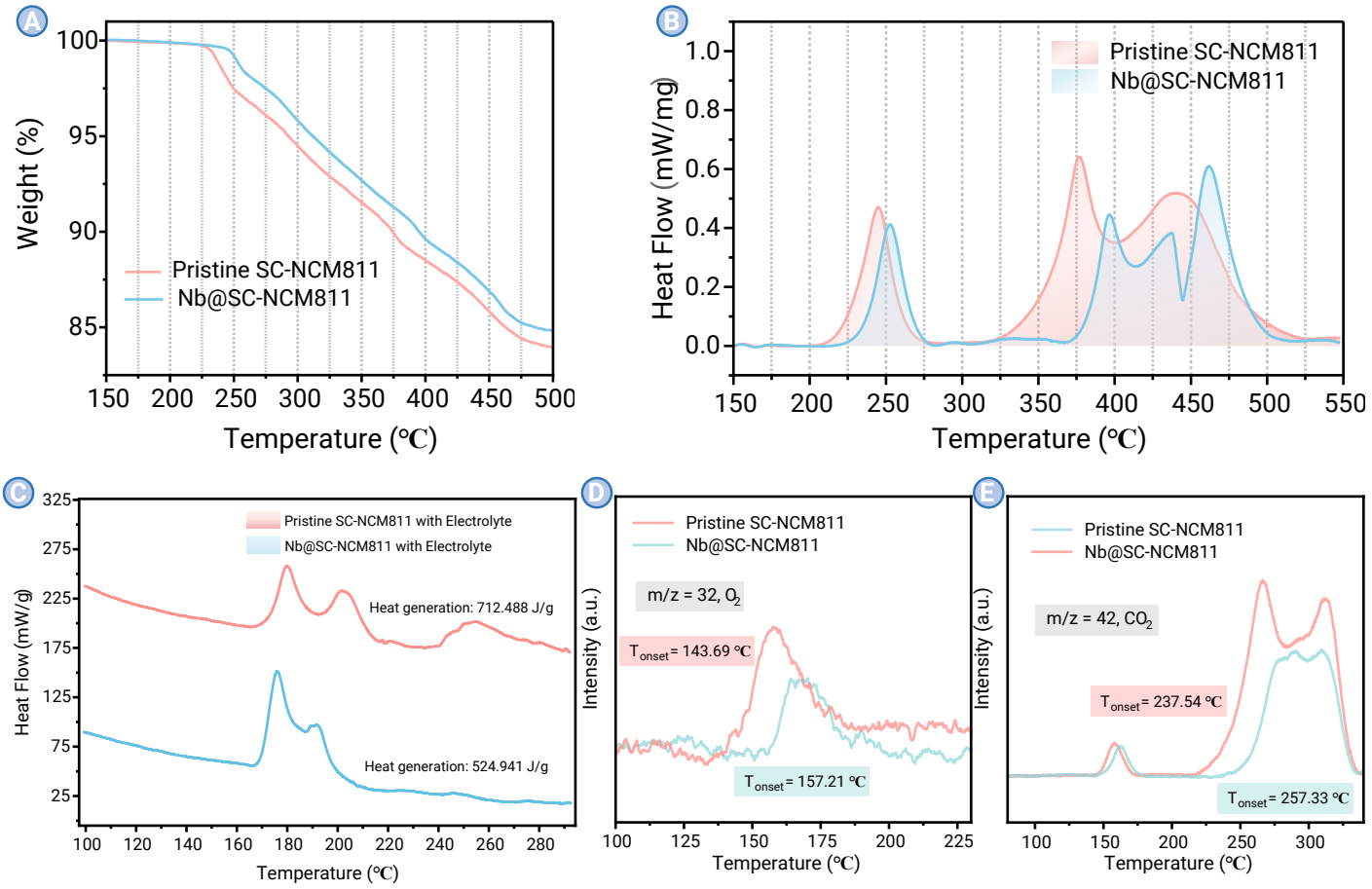

Figure 4. (A) TG curves and (B) DSC curves of delithiated cathode materials. (C) Heat flow curves of the delithiated cathode-electrolyte mixed system by C80 micro-calorimeter. TG/MS results of delithiated cathode materials, (D) O_2, (E) CO_2 signals.

Nb@SC-NCM811 may be attributed to its surface $LiNbO_3$ coating layer, which prevents direct contact between the cathode material and the electrolyte, thereby reducing side reactions and HF corrosion. This would slow down the formation of the cathode electrolyte interphase (CEI) film on the cathode surface during the initial charge and discharge process. Meanwhile, the ion-conducting $LiNbO_3$ coating layer facilitates the rapid migration of lithium ions, and its thickness is reduced to about 2 nm after surface doping, which does not increase the diffusion path of lithium ions.[35] Moreover, a reduced interfacial resistance and an improved lithium-ion diffusion coefficient in Nb-modified SC-NMC811 contribute to enhanced reaction kinetics. The Nb coating also serves to shield the surface of SC-NMC811 from the development of highly ionically resistive phases.[29]

To further investigate the cycling stability and rate performance of the two cathode materials, long-term cycling tests were conducted at 0.5C and 1C. As shown in Figure 3C, the Nb@SC-NCM811, although exhibiting a slightly lower discharge specific capacity than the Pristine SC-NCM811 in the first 20 cycles at 0.5C, demonstrates more stable cycling performance with increasing cycle numbers (> 25 cycles). The Pristine SC-NCM811 shows a discharge specific capacity of 177.44 mAh/g in the first cycle at 0.5C and 138.29 mAh/g after 100 cycles, with a capacity retention rate of 77.90%. Meanwhile, the Nb@SC-NCM811 shows a discharge specific capacity of 173.24 mAh/g in the first cycle at 0.5C and 143.26 mAh/g after 100 cycles, with a capacity retention rate of 82.17%. As shown in Figure 3D, at the rate of 1C, the Nb@SC-NCM811 exhibits a higher discharge specific capacity of 137.28 mAh/g after 100 cycles, maintaining a satisfied capacity retention of 80.33%, which is better than that of the Pristine SC-NCM811 (118.74 mAh/g and 71.26%, respectively). The improved rate performance of Nb@SC-NCM811 can be attributed to the $LiNbO_3$ coating layer on the cathode particle surface, which prevents direct contact between the cathode surface and the electrolyte, reduces interface side reactions and alleviates structural degradation during cycling. Meanwhile, this $LiNbO_3$ coating layer facilitates de-/intercalation kinetics of lithium ions, enhancing the migration rate of lithium ions during charging and discharging. Furthermore, the improved cycling stability of Nb@SC-NCM811 is credited to the surface doping effect of Nb^{5+}. For Nb@SC-NCM811, the surface-doped Nb^{5+} can form stronger Nb-O bonds with oxygen atoms, stabilizing the lattice oxygen at the surface of cathode particles and inhibiting the breakage of TM-O bonds, thus suppressing the release of oxygen and the continuous migration of TM cations into the Li layers during cycling.[20] Moreover, Figure 3E shows two different atomic arrangement patterns in the surface region of Nb@SC-NCM811, labeled as Region I and Region II, respectively. As shown in Figures 3F-I, Region I presents a disordered rock-salt phase structure ($Fm3m$) with 2–5 nm thickness, while Region II is a well-organized layered structure ($R\bar{3}m$). This indicates that the surface doping of Nb^{5+} induced a structural reconstruction of the Nb@SC-NCM811 surface layer, resulting in the formation of a nanometer-thick rock-salt phase shell.[29] This pre-constructed rock-salt phase shell is beneficial for enhancing the structural stability of the cathode particle surface, further protecting the internal layered structure from degradation, making it more difficult for structural degradation during the lithiation and delithiation processes. As shown in Figure 3J, all of cathode materials have similar XRD patterns and display a complete and ordered layered structure, which can be confirmed by the well-splitting of the (006)/(102) and (108)/(110) peaks. As XRD reflects the overall characteristics of the powder samples, the small amount of Nb modification does not significantly influence the XRD patterns of the SC-NCM811 cathode material. But it also can be seen that the (003) peak gradually shifts to the left (lower angle) when the Nb is doped into the SC-NCM811 cathode material. This means that the interlayer spacing is increasing, which may be owning to the stronger electrostatic interaction after the Nb doping.[21,27]

Improved thermal stability of Nb@SC-NCM811

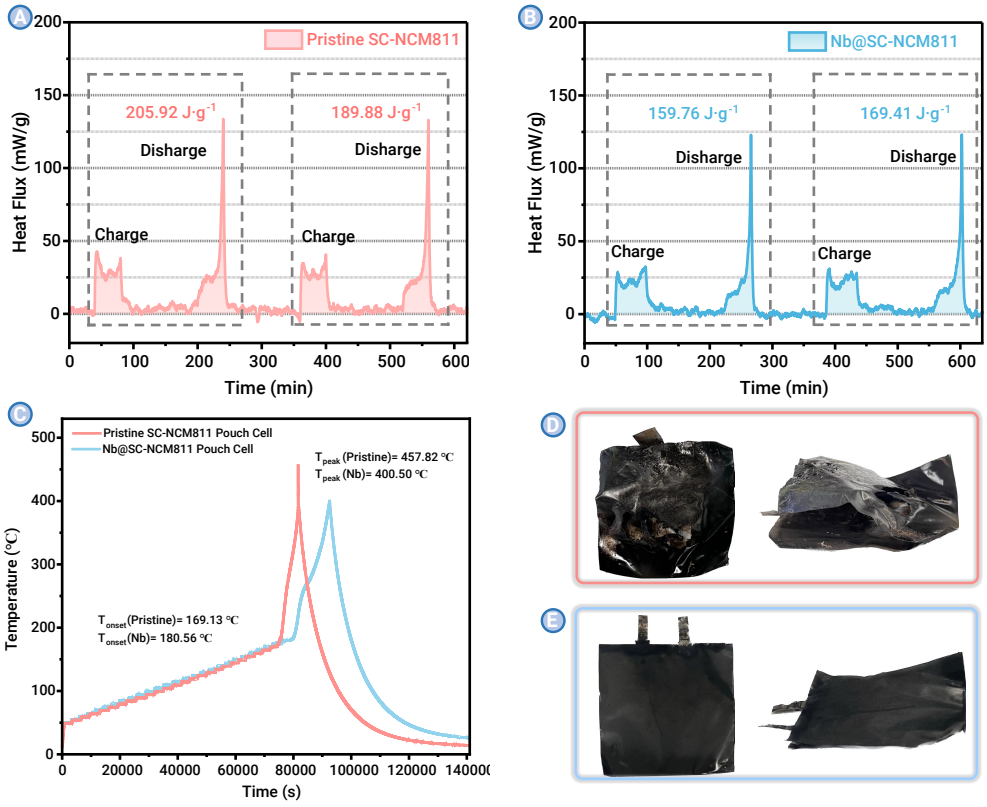

Figure 5. The dynamic heat flow curves of coin batteries during the charge-discharge cycle of (A) Pristine SC-NCM811 and (B) Nb@SC-NCM811. (C) ARC test results of Pristine SC-NCM811 and Nb@SC-NCM811 pouch cells. Morphology of (D) Pristine SC-NCM811 and (E) Nb@SC-NCM811 pouch cell after thermal runaway.

Recent studies indicate that Ni-rich cathode materials are prone to decompose and release oxygen under thermal induction, which reacts with electrolytes and other substances to generate a large amount of heat, rapidly increasing battery temperature and thermal runaway.[36] Therefore, the thermal stability of cathode materials is closely related to the battery safety. As shown in Figure 4A & B, the thermal decomposition behaviors of Pristine SC-NCM811 and Nb@SC-NCM811 are compared using TGA-DSC, and their characteristic thermal parameters are summarized in Table S1. Figure 4A and Table S1 illustrate that Nb@SC-NCM811 starts to lose mass at a higher temperature under thermal induction, indicating that the Nb-modified cathode material is more stable. Additionally, the mass loss of Pristine SC-NCM811 is 16.06%, while that of Nb@SC-NCM811 is 15.16%, suggesting that the latter releases less gas during thermal decomposition at high temperatures. Figure 4B shows that two distinct exothermic peaks exist for both delithiated cathode materials when heated from room temperature to 550 °C. Typically, the heat release in NCM cathode materials is accompanied by oxygen release and crystal structure changes.[6] Therefore, it is inferred that the initial exothermic peak corresponds to the transition of NCM811 cathode materials from a layered to a spinel structure, while the subsequent, more pronounced continuous exothermic peak indicates the transition from a spinel to a rock-salt structure. The onset temperature of the first exothermic peak (T_{onset1}) and the second exothermic peak (T_{onset2}) for Nb@SC-NCM811 are respectively 12.44 °C and 28.91 °C higher than those for Pristine SC-NCM811, and the heat flow peak of Pristine SC-NCM811 occurs earlier and is higher than that of Nb@SC-NCM811. These results demonstrate an improvement in the thermal stability of the Nb-modified Ni-rich cathode material, indicating that $LiNbO_3$ coating and Nb^{5+} surface doping are highly effective for enhancing the thermal stability of Pristine SC-NCM811.

It is believed that the thermal decomposition of NCM cathode materials typically starts from the surface layer of the particles, where oxygen is released under high-temperature induction, forming oxygen vacancies.[37] As the temperature continues to rise, these oxygen vacancies gradually diffuse from the surface to the bulk region, eventually leading to the failure of the entire cathode particle.[37,38] Thus, it can be preliminarily concluded that surface doping of Nb@SC-NCM811 with Nb^{5+} introduces stronger Nb-O bonds, replacing some of the Ni-O bonds and forming a nanometer-thick rock-salt phase shell on the particle surface, thereby better stabilizing the surface layered structure and lattice oxygen.[21] The $LiNbO_3$ coating and Nb^{5+} surface doping can effectively synergize to improve the cathode particle's structural stability, delaying the degradation of its crystal structure at high temperatures, and thereby enhancing the thermal stability of the cathode materials.

Notably, the oxygen released from the thermal decomposition of cathode materials at high temperatures reacts with the electrolyte, which is an important cause of further development of thermal runaway in entire batteries. Therefore, after exploring the thermal stability of cathode materials, the thermal stability of the cathode-electrolyte mixed system was investigated using the C80 micro-calorimeter. As shown in Figure 4C, the Pristine SC-NCM811-electrolyte displays a broader exothermic peak, indicating a more substantial release of oxygen and a more thorough reaction with the electrolyte. Moreover, the heat flow curve of the Nb@SC-NCM811-electrolyte is very flat after 210 °C, while the Pristine SC-NCM811-electrolyte still exhibits exothermic behavior after 240 °C. This indicates that the oxygen release of Nb@SC-NCM811 under thermal induction is alleviated. Hence, within this temperature range, there is insufficient oxygen to react with the electrolyte to release heat. The specific heat generation of the Pristine SC-NCM811-electrolyte is 712.488 J/g, while that of the Nb@SC-NCM811-electrolyte is only 524.941 J/g, which is 73.6% of the former. These results demonstrate a notable improvement in the thermal stability of the Nb@SC-NCM811-electrolyte, which is directly attributable to the $LiNbO_3$ coating and Nb^{5+} surface doping strategy.

Herein, the *in-situ* TG-MS was employed to investigate the gas release behaviors of two delithiated cathode materials under thermal induction. Figure 4D indicates that Pristine SC-NCM811 begins to release oxygen at a lower temperature (143.69 °C), whereas the onset temperature for oxygen release from Nb@SC-NCM811 is higher (157.21 °C), consistent with the conclusions from the TGA-DSC results in Figures 4A & B. It should be noted that acetylene black (with a carbon content greater than 99.5%) is used as a conductive agent in the preparation process of the cathode electrode, so the oxygen released from the cathode after 200 °C reacts with acetylene black to produce carbon dioxide. As illustrated in Figure 4E, compared to Pristine SC-NCM811, the stronger carbon dioxide gas release in Nb@SC-NCM811 is increased by about 20 °C (from 237.54 °C to 257.33 °C). Hence, Nb@SC-NCM811 has a higher onset temperature for thermal decomposition and oxygen release, and a lower total amount of oxygen released. This also explains the absence of significant exothermic peaks in the C80 experiment of Nb@SC-NCM811 after 210 °C.

Enhanced thermal safety performance of Nb@SC-NCM811 battery

In the previous section, our research focuses on the thermal stability of delithiated cathode materials and the cathode-electrolyte mixed system. However, analyzing the thermal behavior of entire LIBs is complex but also more practical. Therefore, the thermal safety of Nb@SC-NCM811 at the cell level was investigated by combining *in-situ* heat generation experiments with coin cells and ARC experiments with pouch cells, thereby verifying the effectiveness of Nb modification of Ni-rich cathode materials in enhancing battery safety performance.

Firstly, dynamic heat generation of two types of coin cells (Pristine SC-

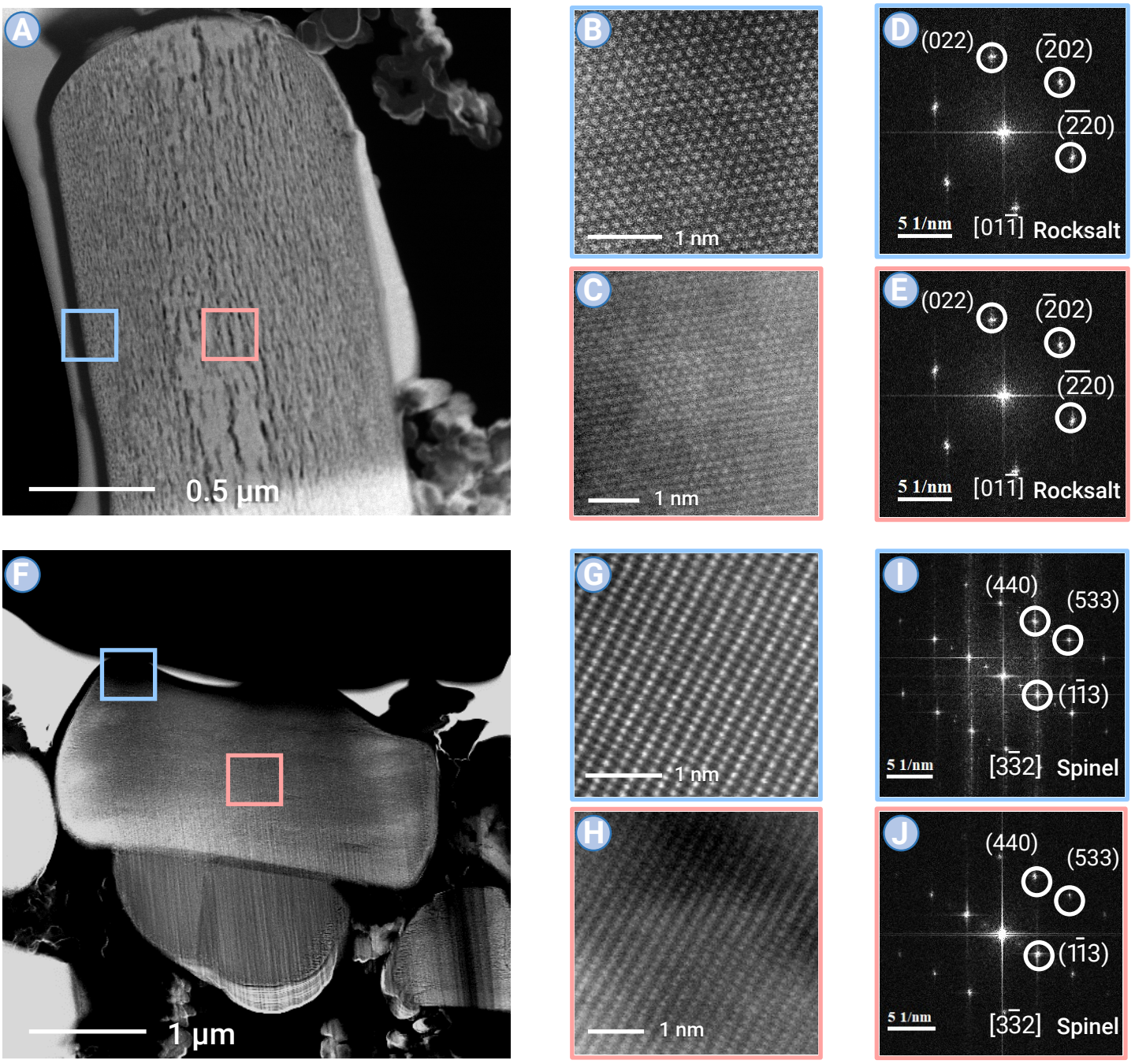

Figure 6. Low-magnification HAADF-STEM image of (A) Pristine SC-NCM811, (F) Nb@SC-NCM811 after thermal failure at 400 °C. Atomic arrangements in the (B & G) surface region and (C & H) bulk region, and corresponding FFT images in the (D & I) surface region and (E & J) bulk region. (A-E) Reproduced with permission.[38] Copyright 2023, Elsevier.

NCM811 and Nb@SC-NCM811) was examined using a MMC with high temperature coin cell module (HTCC). During the charging and discharging processes of the LIBs, the intercalation/deintercalation of lithium ions and the oxidation/reduction of TM ions are accompanied by heat generation. Figure 5A & B show the heat flow curves of Pristine SC-NCM811 and Nb@SC-NCM811 coin cells during *in-situ* charging and discharging cycles. Both curves display the same heat flow trend, with relatively gentle variations throughout the charging process. During the discharging process, the heat flow initially gradually increases, then accelerates sharply, culminating in a pronounced peak towards the end of discharging. Studies indicate that the polarization of the battery becomes more significant at the end of the discharging process, leading to a sudden increase in internal resistance and inducing a rapid increase in irreversible heat, thus presenting a larger exothermic peak.

Furthermore, the dynamic heat generation parameters of the Pristine SC-NCM811 and Nb@SC-NCM811 coin cells are summarized in Table S2. Nb@SC-NCM811 effectively lowers the peak heat flow in coin cells during cycling, suggesting the $LiNbO_3$ coating on Nb@SC-NCM811 improves lithium-ion extraction/insertion. Additionally, the heat generation of Nb@SC-NCM811 is less than that of Pristine SC-NCM811 in the 1st and 2nd cycle periods. Generally, the heat generation during battery cycling is primarily due to the increased impedance and side reactions at the electrode-electrolyte interface. Therefore, it can be inferred that Nb@SC-NCM811 can effectively suppress side reactions between the electrode and the electrolyte, and by promoting the kinetics of lithium ions extraction/insertion, it reduces the irreversible heat and total heat generation during the polarization process, thereby improving the thermal safety of the entire LIB.

Additionally, pouch cells are assembled with Pristine SC-NCM811 and

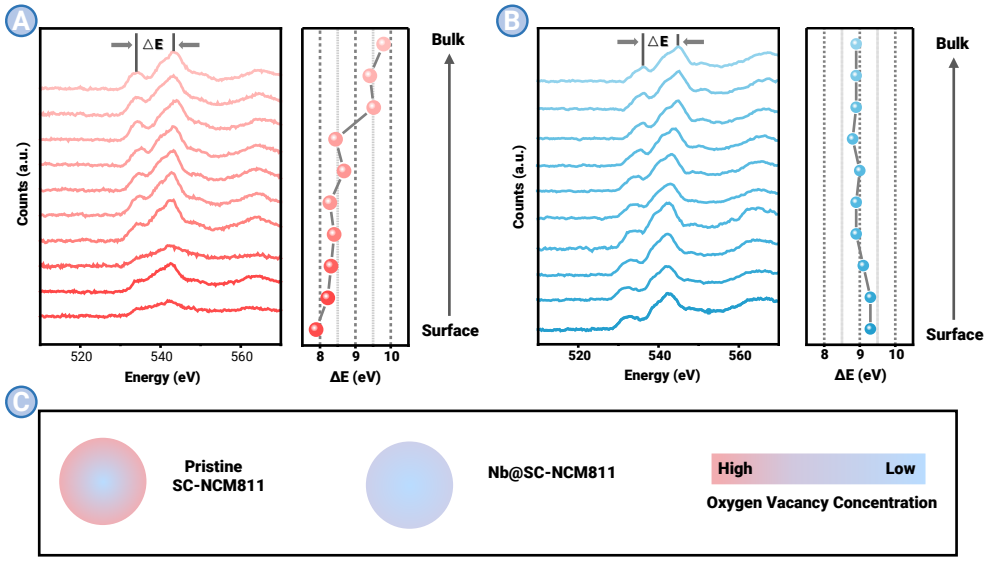

Figure 7. O K-edge spectrum obtained by the EELS line scan results from the surface to the central region of (A) Pristine SC-NCM811 and (B) Nb@SC-NCM811 after heating at 400 °C. (C) Schematic diagram of the oxygen vacancy concentration distribution in Pristine SC-NCM811 and Nb@SC-NCM811 cathode materials.

Nb@SC-NCM811 for comparative experiments on thermal safety. Both pouch cells are charged to 4.2 V (100%SOC) for subsequent accelerating rate calorimetry (ARC) experiments (the pouch cells and the cycling curves are shown in Figure S3). Figure 5C shows that the Pristine SC-NCM811 pouch cell starts a self-heating reaction after 72414 s from the beginning of the experiment, with a starting temperature of 169.13 °C. Subsequently, the battery's temperature rapidly increases, triggering thermal runaway until the reaction ends at a maximum temperature of 457.82 °C. In contrast, the thermal safety performance of the Nb@SC-NCM811 pouch cell is significantly improved. The self-heating reaction of the Nb@SC-NCM811 pouch cell occurs after 79062 s, starting at a temperature of 180.56 °C. This represents an increase of 11.43 °C compared to the Pristine SC-NCM811 pouch cell. Additionally, the temperature curve of the Nb@SC-NCM811 pouch cell is more gradual, and the maximum temperature during thermal runaway (400.50 °C) was 57.32 °C lower than that of the Pristine SC-NCM811 pouch cell. Figures 5D & E respectively show the morphology of the Pristine SC-NCM811 and Nb@SC-NCM811 pouch cells after thermal runaway, demonstrating that the latter suffered less damage, which also corroborates the temperature data from the ARC experiments.

Microscopic mechanism of improved thermal stability in Nb@SC-NCM811

In the previous sections, various thermal analysis methods are employed to demonstrate that the thermal stability of the delithiated Nb@SC-NCM811 has been significantly improved compared to the Pristine SC-NCM811. Meanwhile, the Nb@SC-NCM811 battery shows a significant enhancement in thermal safety during charging and discharging cycles and under external thermal induction. This indicates that the microstructural design of $LiNbO_3$ coating and Nb^{5+} surface doping is practically effective in improving the thermal stability of Ni-rich cathode materials. However, it is necessary to further verify the microscopic mechanism behind the improved thermal stability, providing a more solid theoretical foundation for the design of high-safety Ni-rich cathode materials. Hence, AC-STEM and its equipped electron energy loss spectra (EELS) function are utilized to explore the microstructural evolutions and the concentration distribution of oxygen vacancies within the Pristine SC-NCM811 and Nb@SC-NCM811 after thermal-induced failure at 400 °C. Finally, the underlying mechanisms for the improved thermal stability of SC-NCM811 due to $LiNbO_3$ coating and Nb^{5+} surface doping are revealed by combining the results of DFT calculations.

Observation of structure evolution at the atomic level. Herein, AC-STEM was used to explore the atomic arrangements in the surface layer and bulk region of the cathode particles to investigate the degree of structural degradation. Figure 6 shows the HAADF-STEM images, atomic arrangement images, and corresponding FFT images of Pristine SC-NCM811 and Nb@SC-NCM811 after being heated to 400 °C. Figures 6B-E reveal that both the surface layer and bulk of Pristine SC-NCM811 display the atomic arrangement characteristic of the rock-salt phase, and the results of FFT diffraction pattern indexing also prove the existence of the rock-salt phase. Compared to Pristine SC-NCM811, the results in Figures 6G-J show that Nb@SC-NCM811 has undergone a transition from a layered structure to a spinel structure after being heated to 400 °C, indicating that Nb@SC-NCM811 has better structural stability and can delay the degradation process at high temperatures.

Distribution of oxygen vacancy concentration. The evolution of the lattice structure within NCM cathode materials is intricately associated with the occurrence of oxygen vacancies. As the temperature increases, the formation energy of oxygen vacancies decreases dramatically, and the material surface is more likely to release oxygen and form oxygen vacancies.[9,39] For delithiated Ni-rich cathode materials at a high state of charge, the presence of oxygen vacancies lowers the energy barrier for the migration of TM cations (mainly Ni ions) across layers, leading to the degradation of the layered structure of the cathode material.[39]

As an effective tool for analyzing chemical compositions, EELS can disclose comprehensive information on the atomic electronic states in various materials, encompassing the types of elements, their valence states and concentration distributions, and the atomic radial distribution related to the structure.[40] The concentration distribution of oxygen vacancies in single-crystal cathode particles can be obtained by exploring the changes in the pre-edge peak of the O K-edge at different spatial positions within particles. In the characterization of EELS, oxygen vacancy concentration is determined by the energy position difference ΔE between the pre-edge peak (~532 eV) and the main peak (~542 eV). A smaller ΔE indicates a higher degree of reduction of TM cations and correspondingly more oxygen vacancies. Figures 7A & B show the stacked O K-edge from the surface to the bulk of Pristine SC-NCM811 and Nb@SC-NCM811 after heating to 400 °C. The shape of the O K-edge pre-edge peak at 532 eV, influenced by the hybridization state of the O_{2p} and TM_{3d} orbitals, shifts towards higher energy and diminishes in intensity when TM cations are reduced.[39] As shown in Figure 7A, the intensity of the pre-edge peak of the O K-edge in the surface area of Pristine SC-NCM811 is very low, and the energy difference ΔE is less than 8.5 eV, indicating a high concentration of oxygen vacancies in the surface area. The TM cations in this area are mostly reduced to a lower valence state, leading to severe degradation of the cathode material, which corresponds to the atomic arrangement diagrams and FFT diffraction patterns shown in Figures 6B & D. As the scan extends deeper into the interior of the cathode particle, the pre-edge peak of the O K-edge gradually appears, and the energy difference ΔE gradually increases, first to around 8.5 eV, then surpassing 9.5 eV in the central region.

However, the EELS line scan results from the surface to the bulk of Nb@SC-NCM811 display a different pattern of oxygen vacancy distribution. As shown in Figure 7B, after heating to 400 °C, the pre-edge peak of the O K-edge on the surface of Nb@SC-NCM811 is more obvious, with an energy difference ΔE greater than 9 eV, indicating a much lower concentration of oxygen vacancies. Moreover, as the EELS scan extends more inner, the O K-edge still shows a relatively stable pre-edge peak, with the corresponding ΔE remaining around 9 eV. Although the ΔE in the central region of the cathode particles is slightly higher for Pristine SC-NCM811 than for Nb@SC-NCM811, the average concentration of oxygen vacancies in Nb@SC-NCM811 particles is lower. The above results indicate that surface doping with Nb^{5+} delays the diffusion of oxygen vacancies at high temperatures, reduces the amount of

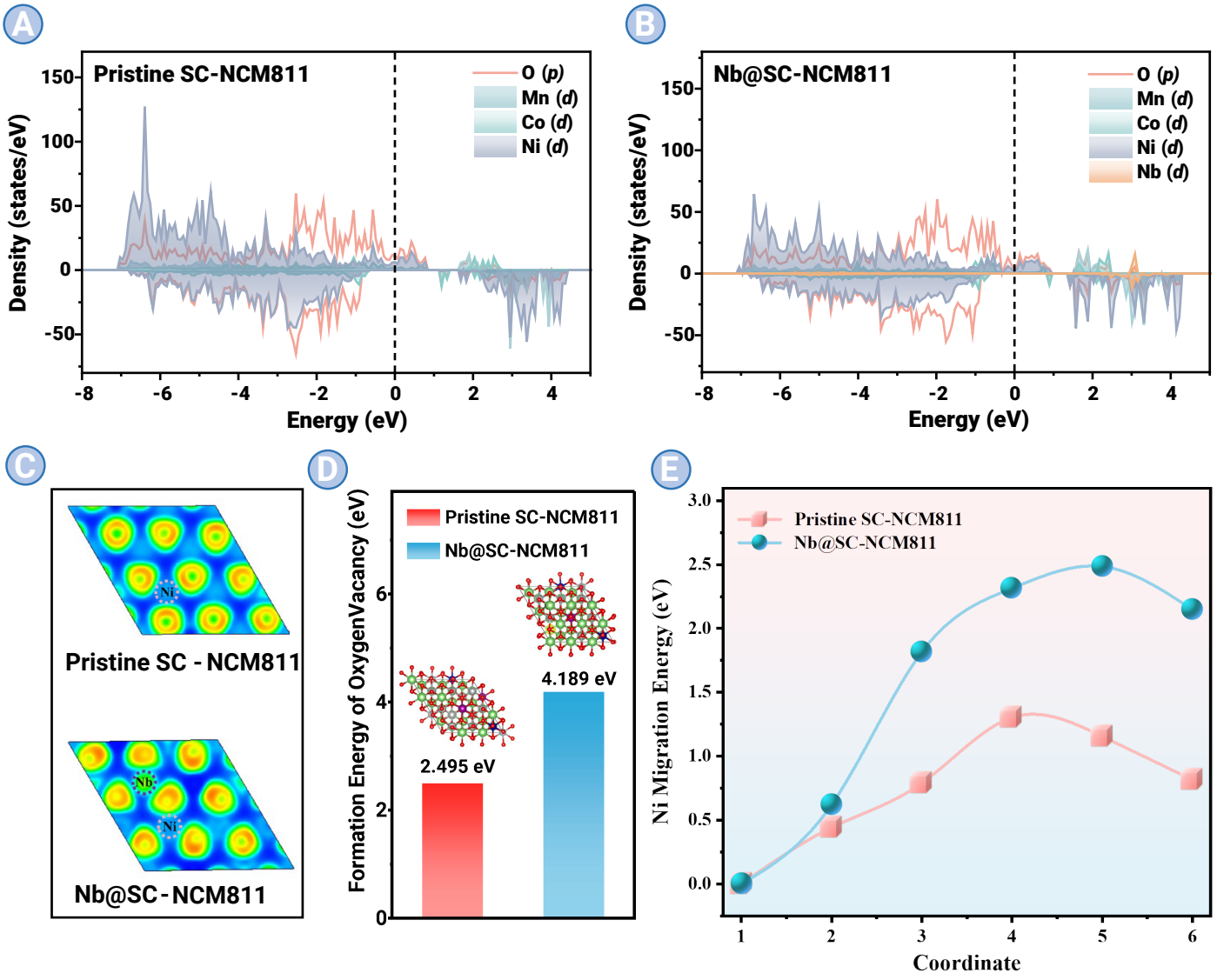

Figure 8. The projected density of states (PDOS) diagram for various elements in (A) Pristine SC-NCM811, (B) Nb@SC-NCM811. (C) Two-dimensional cross-sectional diagrams of the electron localization function (ELF) for Pristine SC-NCM811 and Nb@SC-NCM811. (D) Formation energy of oxygen vacancies in Pristine SC-NCM811 and Nb@SC-NCM811. (E) Energy barrier for cross-layer migration of TM cations.

oxygen released from the NCM811 cathode materials under thermal induction, and thus enhances the thermal stability of the cathode materials as well as the thermal safety of LIBs.

Density function theory (DFT) calculation. To elucidate the underlying mechanism for enhancing thermal stability, theoretical calculations were performed based on first principles using the VASP software, as illustrated in Figure 8. Figures 8A & B reveal that the band gap remains consistent across both doped and undoped materials, suggesting that Nb^{5+} surface doping maintains the electronic structure of the NCM811 cathode material. Additionally, a noticeable decrease in the peak of the Ni element in the conduction band area suggests that the Nb surface doping contributes to the suppression of Li/Ni disorder. The doped material features increased Ni-O-Nb chains, with randomly distributed Nb acting as a shield for the 180° Ni^{2+}-O-Ni^{2+} configurations. This arrangement stabilizes the electronic structure and mitigates Li/Ni disorder, enhancing the structural integrity of the cathode material.

Furthermore, as shown in Figure 8C, the electron localization function (ELF) illustrates that Nb surface doping modifies the chemical environment around oxygen atoms, strengthening Nb-O bonds. This enhancement in bond strength leads to increased electron localization, which is pivotal for the structural stability of NCM cathode material. The strengthened Nb-O interaction suggests a potential for reduced activation barriers for lithium ions, due to the preferential interaction of Nb with oxygen over Ni. Figure 8D reveals that Nb@SC-NCM811 exhibits a significantly higher formation energy (4.189 eV) than Pristine SC-NCM811 (2.495 eV). The elevated formation energy for oxygen vacancies suggests an enhanced thermal and structural stability for NCM811 cathode materials, correlating with a reduced propensity for oxygen release under thermal induction.

As shown in Figure 8E, the energy barrier of TM migration from octahedral to tetrahedral sites in two cathode materials is further confirmed. In Nb@SC-NCM811, the energy barrier of TM migration is significantly increased, which suggests a decreased probability of cross-layer cation migration. Such an increase in the migration barrier reinforces the cathode material's structural framework and potentially extends the material's lifespan by ensuring stable ion transport pathways. This detailed analysis highlights the comprehensive improvements brought about by Nb surface doping in NCM811 cathode materials. It emphasizes the crucial role of Nb^{5+} surface doping in maintaining the electronic structure, enhancing both structural and thermal stability, and thereby boosting the thermal stability of Ni-rich cathode LIBs.

CONCLUSION

This work proposes a structural modification strategy combined with $LiNbO_3$ coating and Nb^{5+} surface doping to enhance the thermal stability of Ni-rich cathode material. The modified Nb@SC-NCM811 cathode material

exhibits better rate capability and cycling stability. Regarding thermal stability, Nb@SC-NCM811 exhibits superior safety characteristics, with a higher decomposition temperature and less oxygen release under thermal induction. At the same time, the maximum heat flow and heat generation in the Nb@SC-NCM811 coin cells during cycling are reduced. The onset temperature of thermal runaway in the assembled pouch cell increases while the peak temperature decreases, reflecting a higher level of overall battery safety. Furthermore, AC-STEM experiments and DFT calculations reveal that the $LiNbO_3$ coating layer reduces the side reactions between the electrolyte and cathode material surface, thereby reducing the heat generation during the battery cycling. The doped Nb^{5+} forms stronger Nb-O bonds in the surface layer of NCM811 cathode particles, enhancing the formation energy of oxygen vacancies and increasing the diffusion barrier of oxygen vacancies from the surface to the bulk region, which delays the release of lattice oxygen and the degradation of the lattice structure of NCM811 cathode material at high temperatures. This study provides a new approach to improving the thermal stability of Ni-rich cathode materials and has significant implications for the microscopic structure design of future high-energy-density cathode materials. Furthermore, improving the safety of LIBs is a multifaceted challenge that involves the thermal stability and compatibility of materials such as cathodes, anodes, electrolytes, and separators. Considering that this study focuses on the safety modification of Ni-rich cathode materials, consistency in the other components was maintained throughout the experiments. However, highly flammable components like organic electrolytes are also critical targets for modification to enhance the safety of LIBs.[41] In future work, Nb-modified cathode materials are planned to be paired with safer electrolyte systems to achieve high-energy-density, high-safety LIBs, thus complying with the trend of high safety development while ensuring excellent electrochemical performance.

REFERENCES

1. Liu L., Li M., Chu L., et al. (2020). Layered ternary metal oxides: Performance degradation mechanisms as cathodes, and design strategies for high-performance batteries. *Prog. Mater. Sci.* **111**:100655. DOI:10.1016/j.pmatsci.2020.100655
2. Liu J., Wang J., Ni Y., et al. (2021). Recent breakthroughs and perspectives of high-energy layered oxide cathode materials for lithium ion batteries. *Mater. Today* **43**:132–165. DOI:10.1016/j.mattod.2020.10.028
3. Zhang S.S. (2020). Problems and their origins of Ni-rich layered oxide cathode materials. *Energy Storage Mater.* **24**:247–254. DOI:10.1016/j.ensm.2019.08.013
4. Wang Y., Feng X., Huang W., et al. (2023). Challenges and Opportunities to Mitigate the Catastrophic Thermal Runaway of High-Energy Batteries. *Adv. Energy Mater.* **13**:2203841. DOI:10.1002/aenm.202203841
5. Noh H.-J., Youn S., Yoon C.S., et al. (2013). Comparison of the structural and electrochemical properties of layered Li[NixCoyMnz]O2 (x = 1/3, 0.5, 0.6, 0.7, 0.8 and 0.85) cathode material for lithium-ion batteries. *J. Power Sources* **233**:121-130. DOI:10.1016/j.jpowsour.2013.01.063
6. Bak, S.M., Hu, E., Zhou, Y., et al. (2014). Structural changes and thermal stability of charged LiNixMnyCozO(2) cathode materials studied by combined in situ time-resolved XRD and mass spectroscopy. *ACS Appl Mater Interfaces* **6**(24):22594–22601. DOI:10.1021/am506712c
7. Wang Q., Mao B., Stoliarov S.I., et al. (2019). A review of lithium ion battery failure mechanisms and fire prevention strategies. *Prog. Energy Combus. Sci.* **73**:95–131. DOI:10.1016/j.pecs.2019.03.002
8. Nam K.-W., Bak S.-M., Hu E., et al. (2013). Combining In Situ Synchrotron X-Ray Diffraction and Absorption Techniques with Transmission Electron Microscopy to Study the Origin of Thermal Instability in Overcharged Cathode Materials for Lithium-Ion Batteries. *Adv. Funct. Mater.* **23**:1047–1063. DOI:10.1002/adfm.201200693
9. Lee E., Muhammad S., Kim T., et al. (2020). Tracking the Influence of Thermal Expansion and Oxygen Vacancies on the Thermal Stability of Ni-Rich Layered Cathode Materials. *Adv. Sci.* **7**:1902413. DOI:10.1002/advs.201902413
10. Alvarado J., Wei C., Nordlund D., et al. (2020). Thermal stress-induced charge and structure heterogeneity in emerging cathode materials. *Mater. Today* **35**:87–98. DOI:10.1016/j.mattod.2019.11.009
11. Huang Q., Li C., Li X., et al. (2024). Multifunction composite phase change material with inorganic flame retardant and organic form stability for improving battery thermal safety. *Innov. Mater.* **2**:100048. DOI:10.59717/j.xinn-mater.2024.100048
12. Li C., Wu Y., Li X., et al. (2024). Flame-retardant composite phase change material with silicone resin and melamine phosphate for battery thermal safety. *Innov. Energy* **1**:100021. DOI:10.59717/j.xinn-energy.2024.100021
13. Wang G., Ping P., Kong D., et al. (2024). Advances and challenges in thermal runaway modeling of lithium-ion batteries. *The Innovation* **5**:100624. DOI:10.1016/j.xinn.2024.100624
14. Li Y., Liu X., Ren D., et al. (2020). Toward a high-voltage fast-charging pouch cell with TiO2 cathode coating and enhanced battery safety. *Nano Energy* **71**:104643. DOI:10.1016/j.nanoen.2020.104643
15. Kim J.W., Travis J.J., Hu E., et al. (2014). Unexpected high power performance of atomic layer deposition coated Li[Ni1/3Mn1/3Co1/3]O2 cathodes. *J. Power Sources* **254**:190–197. DOI:10.1016/j.jpowsour.2013.12.119
16. Wu J., Zuo X., Chen Q., et al. (2019). Functional composite polymer electrolytes with imidazole modified SiO2 nanoparticles for high-voltage cathode lithium ion batteries. *Electrochimica Acta* **320**:134567. DOI:10.1016/j.electacta.2019.134567
17. Huang Y., Chen J., Ni J., et al. (2009). A modified ZrO2-coating process to improve electrochemical performance of Li(Ni1/3Co1/3Mn1/3)O2. *J. Power Sources* **188**:538–545. DOI:10.1016/j.jpowsour.2008.12.037
18. Liu J., Wu Z., Yu M., et al. (2022). Building Homogenous Li(2) TiO(3) Coating Layer on Primary Particles to Stabilize Li-Rich Mn-Based Cathode Materials. *Small* **18**:e2106337. DOI:10.1002/smll.202106337
19. Yin S., Chen H., Chen J., et al. (2022). Chemical-Mechanical Effects in Ni-Rich Cathode Materials. *Chem. Mater.* **34**:1509–1523. DOI:10.1021/acs.chemmater.1c03051
20. Wang B., Zhao H., Cai F., et al. (2022). Surface engineering with ammonium niobium oxalate: A multifunctional strategy to enhance electrochemical performance and thermal stability of Ni-rich cathode materials at 4.5V cutoff potential. *Electrochimica Acta* **403**. DOI:10.1016/j.electacta.2021.139636
21. Zhang C., Wei B., Jiang W., et al. (2021). Insights into the Enhanced Structural and Thermal Stabilities of Nb-Substituted Lithium-Rich Layered Oxide Cathodes. *ACS Appl. Mater. Interfaces* **13**:45619–45629. DOI:10.1021/acsami.1c13908
22. Gao S., Zhan X., and Cheng Y.-T. (2019). Structural, electrochemical and Li-ion transport properties of Zr-modified LiNi0.8Co0.1Mn0.1O2 positive electrode materials for Li-ion batteries. *J. Power Sources* **410-411**:45-52. DOI:10.1016/j.jpowsour.2018.10.094
23. Zhang D., Liu Y., Wu L., et al. (2019). Effect of Ti ion doping on electrochemical performance of Ni-rich LiNi0.8Co0.1Mn0.1O2 cathode material. *Electrochimica Acta* **328**:135086. DOI:10.1016/j.electacta.2019.135086
24. Chu B., You L., Li G., et al. (2021). Revealing the Role of W-Doping in Enhancing the Electrochemical Performance of the LiNi0.6Co0.2Mn0.2O2 Cathode at 4.5 V. *ACS Appl. Mater. Interfaces* **13**:7308-7316. DOI:10.1021/acsami.0c21501
25. Sim S.-J., Lee S.-H., Jin B.-S., et al. (2019). Improving the electrochemical performances using a V-doped Ni-rich NCM cathode. *Sci. Rep.* **9**:8952. DOI:10.1038/s41598-019-45556-7
26. Yang P., Zhang S., Wei Z., et al. (2023). A Gradient Doping Strategy toward Superior Electrochemical Performance for Li-Rich Mn-Based Cathode Materials. *Small* **19**:2207797. DOI:10.1002/smll.202207797
27. Wu H., Zhou X., Yang C., et al. (2023). Concentration-Gradient Nb-Doping in a Single-Crystal LiNi0.83Co0.12Mn0.05O2 Cathode for High-Rate and Long-Cycle Lithium-Ion Batteries. *ACS Appl. Mater. Interfaces* **15**:18828-18835. DOI: 10.1021/acsami.2c23076
28. Kam D., Choi M., Park D., et al. (2023). Unveiling the potential of surface–beneath region doping by induced-diffusion in nickel-rich single crystal cathode for high-performance lithium-ion batteries. *Chem. Eng. J.* **472**:144885. DOI:10.1016/j.cej.2023.144885
29. Xin F., Zhou H., Zong Y., et al. (2021). What is the Role of Nb in Nickel-Rich Layered Oxide Cathodes for Lithium-Ion Batteries. *ACS Energy Lett.* **4**:1377–1382. DOI:10.1021/acsenergylett.1c00190
30. Park N.-Y., Kim S.-B., Kim M.-C., et al. (2023). Mechanism of Doping with High-Valence Elements for Developing Ni-Rich Cathode Materials. *Adv. Energy Mater.* **13**:2301530. DOI:10.1002/aenm.202301530
31. Lee M., Ahmad W., Kim D.W., et al. (2022). Powder Coatings via Atomic Layer Deposition for Batteries: A Review. *Chem. Mater.* **34**:3539–3587. DOI:10.1021/acs.chemmater.1c02944
32. Nano F. (2024). Better materials for a better world. https://www.forgenano.com/.
33. Zhang Q., Cui C., Chen H., et al. (2024). Surface cobaltization for boosted kinetics and excellent stability of nickel-rich layered cathodes. *Nation. Sci. Open* **3**. DOI:10.1360/nso/20240010
34. Li J., Zhu Y., Pang B., et al. (2022). Research on Nb doping–coating composite modification of LiNiO2 cathode material for lithium-ion batteries. *J. Mater. Sci.* **57**:17722–17734. DOI:10.1007/s10853-022-07777-6
35. Liu X., Shi J., Zheng B., et al. (2021). Constructing a High-Energy and Durable Single-Crystal NCM811 Cathode for All-Solid-State Batteries by a Surface Engineering Strategy. *ACS Appl. Mater. Interfaces* **13**(35):41669–41679. DOI:10.1021/acsami.1c11419
36. Cui Z. and Manthiram A. (2023). Thermal Stability and Outgassing Behaviors of High-nickel Cathodes in Lithium-ion Batteries. *Angew. Chem. Int. Ed.* **62**:e202307243. DOI:10.1002/anie.202307243
37. Wei Z., Liang C., Jiang L., et al. (2022). In-depth study on diffusion of oxygen vacancies in Li(NixCoyMnz)O2 cathode materials under thermal induction. *Energy Storage Mater.* **47**:51–60. DOI:10.1016/j.ensm.2022.01.054
38. Wei Z., Liang C., Jiang L., et al. (2023). Probing the thermal degradation mechanism of polycrystalline and single-crystal Li(Ni0.8Co0.1Mn0.1)O2 cathodes from the perspective of oxygen vacancy diffusion. *Energy Storage Mater.* **56**:495-505. DOI:10.

1016/j.ensm.2023.01.029
39. Qian D., Xu B., Chi M., et al. (2014). Uncovering the roles of oxygen vacancies in cation migration in lithium excess layered oxides. *Phys. Chem. Chem. Phys.* **16**:14665–14668. DOI:10.1039/c4cp01799d
40. Roychoudhury S., Qiao R., Zhuo Z., et al. (2020). Deciphering the Oxygen Absorption Pre - edge: A Caveat on its Application for Probing Oxygen Redox Reactions in Batteries. *Energy Environ. Mater.* **4**:246–254. DOI:10.1002/eem2.12119
41. Guan D., Hu G., Peng Z., et al. (2022). A nonflammable low-concentration electrolyte for lithium-ion batteries. *J. Mater. Chem. A* **10**(2:12575-12587. DOI:10.1039/d2ta01760a

FUNDING AND ACKNOWLEDGMENTS

This work is supported by the National Natural Science Foundation of China (No. 52204248), Chinese Academy of Sciences (CAS) Project for Young Scientists in Basic Research (YSBR-098), Opening Fund of State Key Laboratory of Fire Science (SKLFS) under Grant No. HZ2024-KF16 and Engineering Laboratory of Battery Safety and Accident Control of Petroleum and Chemical Industry (No. ELBSAC202304). This work was partially carried out at the USTC Center for Micro and Nanoscale Research and Fabrication. The authors would like to thank Shengquan Fu and Hongmin Zhou from the SEM group, Instrument Center for Physical Science, University of Science and Technology of China, for assisting with the SEM experiments. The authors also thank the BL12B station of the National Synchrotron Radiation Laboratory (NRSL) in Hefei for sXAS measurements.

AUTHOR CONTRIBUTIONS

All authors contributed to the manuscript and approved the final version.

DECLARATION OF INTERESTS

The authors declare no competing interests.

DATA AND MATERIALS AVAILABILITY

Data are available from the corresponding author upon reasonable request.

SUPPLEMENTAL INFORMATION

Supplementary materials are available at: https://doi.org/10.59717/j.xinnenergy.2025.100083